nature energy

ARTICLES

https://doi.org/10.1038/s41560-017-0057-0

Enhancing long-term photostability of $BiVO_4$ photoanodes for solar water splitting by tuning electrolyte composition

Dong Ki Lee and Kyoung-Shin Choi*

As the performance of photoelectrodes used for solar water splitting continues to improve, enhancing the long-term stability of the photoelectrodes becomes an increasingly crucial issue. In this study, we report that tuning the composition of the electrolyte can be used as a strategy to suppress photocorrosion during solar water splitting. Anodic photocorrosion of $BiVO_4$ photoanodes involves the loss of V^{5+} from the $BiVO_4$ lattice by dissolution. We demonstrate that the use of a V^{5+}-saturated electrolyte, which inhibits the photooxidation-coupled dissolution of $BiVO_4$, can serve as a simple yet effective method to suppress anodic photocorrosion of $BiVO_4$. The V^{5+} species in the solution can also incorporate into the FeOOH/NiOOH oxygen-evolution catalyst layer present on the $BiVO_4$ surface during water oxidation, further enhancing water-oxidation kinetics. The effect of the V^{5+} species in the electrolyte on both the long-term photostability of $BiVO_4$ and the performance of the FeOOH/NiOOH oxygen-evolution catalyst layer is systematically elucidated.

Recently, $BiVO_4$ has been identified as one of the most promising oxide-based photoanodes for use in a photoelectrochemical cell (PEC) for water splitting due to its uniquely advantageous features[1–4]. In general, polycrystalline oxide-based photoelectrodes are known to suffer from poor charge transport properties (for example, short carrier diffusion length) and fast bulk and surface electron–hole recombination. However, recent studies have shown that the charge transport properties and electron–hole separation in $BiVO_4$ can be easily improved with composition tuning (for example, doping of the V site with W (refs [5–7]), Mo (refs [5,7–10]) or P (ref. [11]), increasing oxygen vacancies[12,13]) and morphology tuning[14,15]. Furthermore, when coupled with proper oxygen-evolution catalysts (OECs)[14,16–18], the surface recombination of $BiVO_4$ photoanodes during photooxidation of water can become negligible even at potentials close to the flatband potential of $BiVO_4$. As a result, the photocurrent onset potential of a $BiVO_4$/OEC photoanode for water oxidation can be very near its flatband potential. This, when combined with its conduction band minimum located very near the H_2-evolution potential, allows a $BiVO_4$/OEC photoanode to achieve a photovoltage of ~1 V for water oxidation (that is, the difference between the photocurrent onset potential and the thermodynamic potential for water oxidation)[14]. This feature, along with the various inexpensive routes to produce $BiVO_4$ electrodes, has made $BiVO_4$ one of the most frequently used photon absorbers for recently developed PECs capable of unassisted solar water splitting[19–22].

The fundamental limitation of $BiVO_4$ is its relatively large bandgap (2.4–2.5 eV). However, a recent study utilizing Fe_2O_3 and $BiVO_4$ as dual photoanodes achieved a solar-to-hydrogen conversion efficiency of 7.7% (ref. [22]). This result showed that even though Fe_2O_3 has a smaller bandgap than $BiVO_4$, having $BiVO_4$ and Fe_2O_3 together results in a higher photocurrent than Fe_2O_3 alone. This suggests that even when a photoanode with a smaller bandgap than Fe_2O_3 is identified, keeping $BiVO_4$ as one of the photon absorbers in the multi-photon absorber PECs may be advantageous if the smaller-bandgap photoanode cannot utilize photons with energy greater than 2.4 eV as efficiently as $BiVO_4$.

As the performance of $BiVO_4$-based photoanodes continues to improve, the photostability of $BiVO_4$ becomes an important issue[23,24]. To date, photocorrosion of photoelectrodes has been prevented by using two different methods. The first method is to place a protection layer on the photoelectrode[24–26]. When a photoelectrode is photocorroded, the change in oxidation state of one or more of the elements in the photoelectrode must be coupled with a change in the coordination of the element, which involves the removal or addition of atoms. Since this change occurs at the semiconductor/electrolyte interface, the electrolyte serves as an acceptor or a donor of the atoms necessary for photocorrosion to occur (for example, accepting O from Cu_2O during cathodic photocorrosion of Cu_2O to Cu). Therefore, if the photoelectrode is coated with an inert layer such as TiO_2 and is not in direct contact with the electrolyte, the photocorrosion cannot occur even if holes or electrons are available.

The second method to suppress photocorrosion is the use of a catalyst layer that increases the rate of interfacial charge transfer[27]. For a semiconductor that is not thermodynamically stable against photocorrosion, the degree of photocorrosion critically depends on the relative rate of photocorrosion compared with the rates of interfacial charge transfer and surface recombination. If the interfacial charge transfer rate or surface recombination rate is significantly faster than that of photocorrosion, photocorrosion can be kinetically suppressed. This is why a catalyst layer, which improves the rate of interfacial charge transfer, can kinetically suppress photocorrosion[17].

In this study, we propose a strategy to suppress photocorrosion that can complement the previously reported methods. The anodic photocorrosion of $BiVO_4$ involves the loss of V^{5+} ions from the $BiVO_4$ lattice by dissolution. We demonstrate that the use of a V^{5+}-saturated electrolyte that inhibits the photooxidation-coupled dissolution of V^{5+} from $BiVO_4$ offers a simple but effective strategy to suppress anodic photocorrosion of $BiVO_4$. We also report the effect of the V^{5+} species in the electrolyte on the oxygen-evolution performance of the FeOOH/NiOOH OECs present on the $BiVO_4$ surface. This investigation provides insights into preventing photocorrosion

Department of Chemistry, University of Wisconsin-Madison, Madison, WI, USA. *e-mail: kschoi@chem.wisc.edu

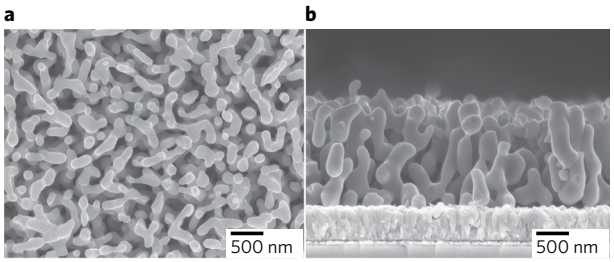

Fig. 1 | Morphology of nanoporous $BiVO_4$ electrode. a,**b**, Top-view (**a**) and side-view (**b**) SEM images of a nanoporous $BiVO_4$ electrode used in this study.

of photoelectrodes involving dissolution and improving catalytic performances of OECs by tuning electrolyte composition.

Preparation of $BiVO_4$ photoanodes

The $BiVO_4$ used in this study was prepared on the basis of the method reported in a recent study where an electrodeposited BiOI film was used as a precursor film to form a nanoporous $BiVO_4$ electrode[14,28]. A few modifications made to the synthesis, which enabled a higher nucleation density and more uniform growth of BiOI (Supplementary Fig. 1), are described in the Methods.

The scanning electron microscopy (SEM) images of the resulting nanoporous $BiVO_4$ electrodes are shown in Fig. 1. Compared with $BiVO_4$ photoelectrodes prepared using previously reported methods (Supplementary Fig. 2), the $BiVO_4$ electrodes used in this study are composed of denser and thicker columnar particles of $BiVO_4$ with a more uniform film front.

The resulting $BiVO_4$ films were re-annealed at 350 °C for 2 h in a tube furnace while flowing N_2, which has been demonstrated previously to simultaneously enhance the photon absorption and charge transport properties of $BiVO_4$ (ref. [13]). Then, FeOOH and NiOOH OEC layers were consecutively photodeposited on the $BiVO_4$ electrodes. The X-ray diffraction (XRD) pattern of bare $BiVO_4$ (Supplementary Fig. 3) and the SEM image of a $BiVO_4$/FeOOH/NiOOH electrode (Supplementary Fig. 4) can be found in the Supplementary Information.

We note that the chemical and photoelectrochemical instability of polycrystalline $BiVO_4$ electrodes caused by dissolution depends critically on the quality of the $BiVO_4$ electrodes. $BiVO_4$ electrodes that contain poorly crystalline particles with poor adhesion both between $BiVO_4$ particles and at the $BiVO_4$/substrate interface, especially with easily soluble amorphous impurities at the interfaces (that is, V_2O_5 or vanadium-rich regions), can readily dissolve or disintegrate under conditions where high-quality $BiVO_4$ electrodes would be stable. This is why conflicting results have been reported regarding the chemical and photoelectrochemical stabilities of $BiVO_4$ photoelectrodes produced via different synthesis methods[23,29]. To obtain a fair and accurate stability assessment of $BiVO_4$, the use of a high-quality $BiVO_4$ electrode, which is free from the aforementioned factors that result in the underestimation of the stability, is critical. The $BiVO_4$ electrodes used in this study, which went through a 30 min immersion process in 1 M NaOH to completely remove V_2O_5, did not show any changes in morphology, crystallinity, photon absorption or photocurrent generation before and after immersion in a pH 9 solution for 50 days (Supplementary Fig. 5). These electrodes enabled us to examine the photon-induced instability of $BiVO_4$ electrodes that are otherwise chemically stable in a pH 9 solution.

Photoelectrochemical performance and stability of $BiVO_4$

The *J*–*V* plot of the resulting $BiVO_4$/FeOOH/NiOOH photoanode for photooxidation of water was obtained in a 1.0 M potassium

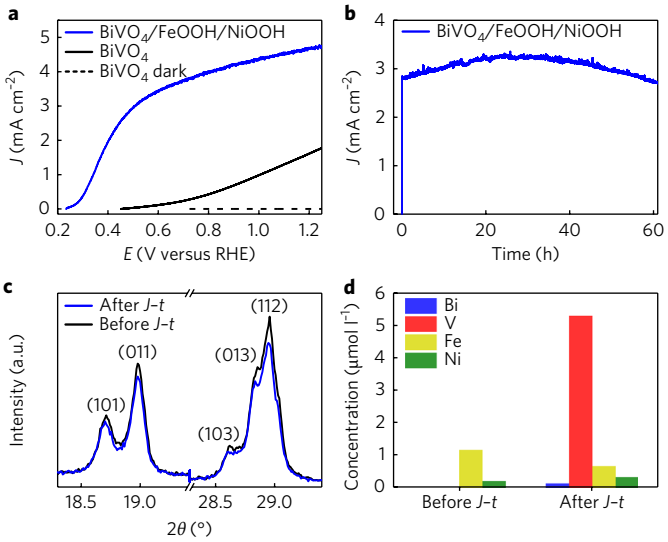

Fig. 2 | Performance and stability of $BiVO_4$/FeOOH/NiOOH. a, *J*–*V* plot of $BiVO_4$ (black) and $BiVO_4$/FeOOH/NiOOH (blue) measured in KB solution (AM 1.5 G, 100 mW cm^{-2} illumination; scanning rate of 10 mV s^{-1}). The dark current of bare $BiVO_4$ is shown as a black dashed line. **b**, *J*–*t* plot of $BiVO_4$/FeOOH/NiOOH at 0.6 V versus RHE in KB solution. **c**, XRD patterns of $BiVO_4$ before (black) and after (blue) 60 h *J*–*t* measurement in KB solution. **d**, ICP analysis of KB solution before and after 60 h *J*–*t* measurement.

borate buffer (pH 9.3), referred to as KB solution hereafter (Fig. 2a). For comparison, the *J*–*V* plot of the bare $BiVO_4$ photoanode is also shown. The effect of the OEC layer on enhancing the photocurrent for water oxidation is clear from this figure. When the FeOOH/NiOOH layer is present, the photocurrent onset is shifted from 0.47 ± 0.06 V to 0.24 ± 0.03 V versus RHE (reversible hydrogen electrode) and the photocurrent rapidly increases to 2.0 mA cm^{-2} at a potential as low as 0.40 V versus RHE, exhibiting an excellent fill factor. The photocurrent densities measured at 0.60 V and 1.23 V versus RHE are 3.4 ± 0.2 mA cm^{-2} and 4.7 ± 0.3 mA cm^{-2}, respectively.

The *J*–*t* plot of the $BiVO_4$/FeOOH/NiOOH photoanode measured at 0.6 V versus RHE shows that the photocurrent gradually increases for about 20 h and then decreases after about 40 h, indicating that this film is not completely photostable over an extended period of time (Fig. 2b). The SEM study on the $BiVO_4$/FeOOH/NiOOH photoanode before and after 60 h of the *J*–*t* measurement showed an indication of $BiVO_4$ dissolution (Supplementary Fig. 6). The comparison of the XRD patterns of $BiVO_4$ before and after the *J*–*t* measurement for 60 h also shows a decrease in the intensity of the diffraction peaks after the *J*–*t* measurement, confirming a slight dissolution loss of $BiVO_4$ (Fig. 2c).

The electrolyte used for the *J*–*t* measurement was also analysed using inductively coupled plasma optical emission spectrometry (ICP–OES). The ICP–OES results indeed show the presence of both Bi and V in the electrolyte after the *J*–*t* measurement. The concentration of V (5.30 μmol l^{-1}) is significantly higher than that of Bi (0.14 μmol l^{-1}) (Fig. 2d), suggesting that vanadium leaching from $BiVO_4$ is the major compositional change that results from anodic photocorrosion.

Any compositional change caused by the anodic photocorrosion of $BiVO_4$ must be linked with the oxidation of one or more of the elements present in $BiVO_4$. As V^{5+} in the $BiVO_4$ lattice cannot be further oxidized, the dissolution of V^{5+} must be coupled with the photooxidation of Bi^{3+} and/or lattice oxide (O^{2-}) ions. When the surface-accumulated holes are localized on the Bi^{3+} or O^{2-} ions, which can initiate photocorrosion of $BiVO_4$, the corresponding

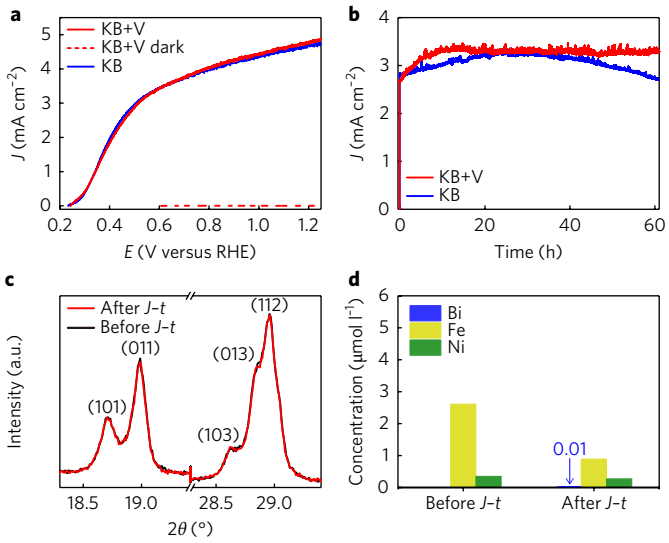

Fig. 3 | Effect of V^{5+} in the electrolyte on the performance and stability of $BiVO_4$/FeOOH/NiOOH. a,**b**, *J*–*V* plots (**a**) and *J*–*t* plots (**b**) at 0.6 V versus RHE of $BiVO_4$/FeOOH/NiOOH film in KB (blue) and KB + V (red) solution (AM 1.5 G, 100 mW cm^{-2} illumination; scanning rate of 10 mV s^{-1}). The dark current of $BiVO_4$/FeOOH/NiOOH in KB + V is shown as a red dashed line in **a**. **c**, XRD patterns of $BiVO_4$ before (black) and after (red) 60 h *J*–*t* measurement in KB + V solution. **d**, ICP analysis of KB + V solution before and after 60 h *J*–*t* measurement. The concentration of V, which is 200 mM, is not shown in the plot because its magnitude causes the changes in the other species' concentrations to be indiscernible.

change in the local structure around these ions may destabilize the $BiVO_4$ lattice and increase the solubility of $BiVO_4$ at the surface. Then, the dissolution of V^{5+} would be dominant because V^{5+} is significantly more soluble than Bi^{3+} in a pH 9 solution[30].

When the *J*–*t* measurement of a bare $BiVO_4$ electrode was obtained for the photooxidation of sulfite, which has fast oxidation kinetics, a stable photocurrent was generated for 500 h without any sign of mass or crystallinity loss or photocorrosion (Supplementary Fig. 7). This indicates that as long as the surface-reaching holes are consumed quickly for the interfacial oxidation reaction and are not accumulated at the surface, $BiVO_4$ can be photostable. However, the photocurrent for water oxidation achieved by the $BiVO_4$/FeOOH/NiOOH photoanode (Fig. 2a) is only 80% of the photocurrent for sulfite oxidation achieved by the bare $BiVO_4$ photoanode (Supplementary Fig. 8). This means that ~20% of the surface-reaching holes are lost either to surface recombination or to anodic photocorrosion during water oxidation. The instability of the photocurrent shown in Fig. 2b suggests that at least a portion of the surface-reaching holes were used for photocorrosion.

Effect of a V^{5+}-saturated electrolyte on the photostability

As we were unable to identify OEC layers that can increase the photocurrent for water oxidation to the level of sulfite oxidation, we investigated a strategy that can suppress photocorrosion by retarding the rate of photocorrosion. We postulated that if the photooxidation of $BiVO_4$ and the dissolution of V^{5+} are coupled and the dissolution of V^{5+} is critical for subsequent steps of the photocorrosion process, the photocorrosion rate of $BiVO_4$ may be significantly decreased by suppressing the dissolution of V^{5+} from $BiVO_4$ through the use of a V^{5+}-saturated electrolyte via Le Châtelier's principle. If the rate of photocorrosion can be made considerably slower so that all the surface-reaching holes are used by water oxidation and surface recombination instead, photocorrosion of $BiVO_4$ can be suppressed.

We note that this strategy is different from the self-healing mechanism reported for Co–Pi OECs[31]. During oxygen-evolution reaction (OER), the oxidation state of Co cycles between +2, +3 and +4, and the soluble Co^{2+} can leach out from the catalyst layer to a pH 7 phosphate buffer solution[31]. However, the Co^{2+} can be oxidized to insoluble Co^{3+} and re-deposited as Co–Pi by the anodic bias applied during water oxidation. This self-healing mechanism does not suppress Co^{2+} dissolution but rather enables the reformation of Co–Pi though a separate reaction after the Co^{2+} dissolution occurs. On the other hand, the oxidation state of V in $BiVO_4$ is invariably 5+, and the dissolution of V^{5+} is caused by the photooxidation of $BiVO_4$. Our strategy is to inhibit the dissolution of V^{5+}, which is coupled with photooxidation of $BiVO_4$, as a means to make the rate of photocorrosion slower than those of water oxidation and surface recombination, thereby suppressing photocorrosion.

To verify this postulation, we pre-saturated the pH 9 borate buffer with V_2O_5. V_2O_5 is soluble and forms $H_2VO_4^-$ and HVO_4^{2-} species in a pH 9 aqueous medium[30]. However, we found that the presence of 1.0 M borate buffer significantly lowers the solubility of V_2O_5 and the solution becomes saturated at a concentration of 0.1 M V_2O_5. Therefore, 1.0 M borate buffer containing 0.1 M V_2O_5, referred to as a KB + V solution hereafter, was used as the electrolyte.

The *J*–*V* and *J*–*t* plots of $BiVO_4$/FeOOH/NiOOH measured in the KB + V solution are shown in Fig. 3a,b in comparison with those measured in the KB solution. The *J*–*V* plots measured in the KB and KB + V solutions look identical, suggesting that the presence of $H_2VO_4^-$/HVO_4^{2-} species does not interfere with the interfacial charge transfer of holes from $BiVO_4$ to water. The *J*–*t* plot shows that the photocurrent density gradually rises to 3.2 ± 0.2 mA cm^{-2} during the first 10 h and is maintained for 50 h, suggesting that photocorrosion is suppressed with the addition of V_2O_5 to the electrolyte (Fig. 3b).

The XRD pattern of the $BiVO_4$/FeOOH/NiOOH photoanode shows that the intensity of the diffraction peaks of $BiVO_4$ remains unchanged after 60 h of *J*–*t* measurement when V_2O_5 is present in the solution (Fig. 3c). Furthermore, the ICP result shows that the amount of Bi present in the KB + V solution after the *J*–*t* measurement is negligible (0.01 μmol l^{-1}), suggesting that the presence of V_2O_5 in the electrolyte effectively suppressed the dissolution of $BiVO_4$ (Fig. 3d). (The change in V could not be accurately measured because the solution was already saturated with V_2O_5.) Both the XRD and ICP results clearly support that the pre-saturation of the electrolyte with V^{5+} can serve as an effective strategy to suppress anodic photocorrosion of $BiVO_4$.

The Faradaic efficiency for photoelectrochemical O_2 and H_2 evolution by the $BiVO_4$/FeOOH/NiOOH photoanode in the KB + V solution was ~100% (Supplementary Fig. 9), which confirmed that the presence of $H_2VO_4^-$ and HVO_4^{2-} species does not interfere with the water oxidation or reduction reactions. This could also be confirmed by comparing the linear sweep voltammograms (LSVs) performed in the KB and KB + V solutions in the dark to observe electrochemical water oxidation and water reduction. The LSVs obtained in the two solutions look identical, meaning that any redox reactions of $H_2VO_4^-$ and HVO_4^{2-} species do not occur between the water oxidation and reduction potentials (Supplementary Fig. 10).

Effect of a V^{5+}-saturated electrolyte on OEC layers

We also examined the possibility that the presence of V^{5+} species in the electrolyte may affect the composition and/or the performance of the FeOOH/NiOOH OEC layer during water oxidation. As the incorporation of vanadium into the OEC layer present on the $BiVO_4$ surface is difficult to investigate due to the abundance of vanadium in the underlying $BiVO_4$ film, we prepared a FeOOH/NiOOH film on a fluorine doped-tin oxide (FTO) substrate with a thickness and composition comparable to that of the FeOOH/NiOOH layer on $BiVO_4$. The performance and stability of the resulting film was

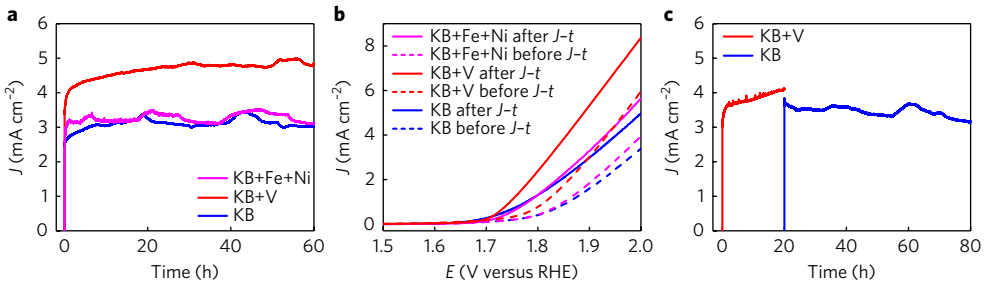

Fig. 4 | Effect of V^{5+} in the electrolyte on the OEC layer. a, *J–t* plots of the FeOOH/NiOOH film on FTO in KB (blue), KB + V (red) and KB + Fe + Ni (pink) solutions at 1.9 V versus RHE. **b**, LSVs of the FeOOH/NiOOH film on FTO before (dashed lines) and after (solid lines) 60 h *J–t* measurement. **c**, *J–t* plots of the FeOOH/NiOOH film on FTO in KB + V solution for 20 h (red) followed by 60 h in the KB solution (blue).

tested by performing a *J–t* measurement at 1.9 V versus RHE for 60 h in the KB and KB + V solutions for comparison. The applied potential of 1.9 V versus RHE was selected to mimic the photocurrent density achieved by the $BiVO_4$/FeOOH/NiOOH electrode shown in Fig. 2b.

The *J–t* plot of the FeOOH/NiOOH electrode measured in the KB solution shows a stable current density of 3.0 mA cm^{-2} for 60 h (Fig. 4a), which confirms that the instability of the photocurrent shown in Fig. 2b is not due to the loss of the mass or activity of the FeOOH/NiOOH layer. When the same reaction was repeated in the KB + V solution, not only was the stability of the current maintained, but also a significant enhancement in current density up to 5.0 mA cm^{-2} was observed, suggesting that vanadium was incorporated into the surface of the OEC layer and favourably affected the catalytic performance for O_2 evolution.

The composition change of the FeOOH/NiOOH electrode before and after the *J–t* measurement was analysed by energy-dispersive X-ray spectroscopy (EDS). In general, EDS analysis is not appropriate for a quantitative analysis of electrodes that contain multiple phases whose composition is not uniform throughout the film. However, the FeOOH/NiOOH films analysed in this study were very thin and uniform, and we ensured that the Sn signal from the underlying FTO substrate was consistent for all measurements. This allowed us to confirm that the amount of sample analysed and the penetration depth of the X-ray beam for all measurements were consistent. Therefore, the EDS results in Supplementary Table 3, which show the relative atomic ratios of the elements (Fe, Ni and V) compared with Sn, could reasonably be used to evaluate the relative gain and loss of each element during the *J–t* measurement.

The EDS results show that after the *J–t* measurement in the KB solution, the content of Fe in the OEC layer increased slightly. This is due to the Fe impurity present in the KOH and H_3BO_3 used to prepare the KB solution (Fig. 2d), which gets incorporated into the FeOOH/NiOOH OEC layer during water oxidation. When the *J–t* measurement of the FeOOH/NiOOH film was performed in the KB + V solution, a significant level of incorporation of vanadium into the film was observed, with the atomic ratio of Fe/Ni/V being 5:1:1. This confirms that the enhanced catalytic performance shown in Fig. 4a is indeed due to the incorporation of vanadium. We also found that the content of Fe and Ni in this film was higher than that in the FeOOH/NiOOH film operated in the KB solution. This is because the V_2O_5 used to prepare the KB + V solution also contained Fe and Ni impurities, and, therefore, the concentrations of Fe and Ni ions in the KB + V solution were higher than those in the KB solution (Fig. 3d). The concentrations of Fe and Ni ions in the KB + V solution were 2.63 μmol l^{-1} and 0.38 μmol l^{-1}, respectively, while in the KB solution they were 1.18 μmol l^{-1} and 0.22 μmol l^{-1}, respectively.

To exclude the possibility that the higher current shown in the KB + V solution is due to the incorporation of more Fe and Ni into the film rather than the incorporation of V, we also obtained a *J–t* plot of the FeOOH/NiOOH film in a KB solution after adding an additional 1.50 μmol l^{-1} Fe^{2+} and 0.20 μmol l^{-1} Ni^{2+} without vanadium (referred to as a KB + Fe + Ni solution hereafter) in order to achieve comparable concentrations of Fe^{2+} and Ni^{2+} to those in KB + V. Figure 4a shows that the current density observed in the KB + Fe + Ni solution is comparable to that observed in the KB solution. The elemental analysis of the FeOOH/NiOOH electrode after the *J–t* measurement in the KB + Fe + Ni solution showed more Fe and Ni than the FeOOH/NiOOH electrode operated in the KB solution but less Fe and Ni than the FeOOH/NiOOH electrode operated in the KB + V solution. These results suggest that the current enhancement shown in the KB + V solution is truly due to the incorporation of vanadium into the film and that the vanadium incorporation also facilitates the incorporation of more Fe and Ni. This means that the new phase formed in situ on the FeOOH/NiOOH electrode surface during water oxidation is either a mixture of ternary phases (Ni–V–O and Fe–V–O) or a quaternary phase (Fe–Ni–V–O).

LSVs of the FeOOH/NiOOH electrode in KB, KB + V and KB + Fe + Ni solutions before and after the *J–t* measurement for 60 h are shown in Fig. 4b. All of the films showed enhanced performances after the *J–t* measurement. This was expected on the basis of the gradual increase in the current density observed during the first few hours of the *J–t* measurement when the catalyst surface was optimally restructured or activated for water oxidation. Among these, the film operated in the KB + V solution showed the most pronounced increase in the current density due to the incorporation of vanadium achieved during the *J–t* measurement.

Although further studies are required to better understand the nature of the interfacial vanadium phase formed on the FeOOH/NiOOH layer, the effect of vanadium on enhancing the OER catalytic performance of Ni-based OECs has been reported previously[32]. The water oxidation mechanism is believed to be composed of four steps: the formation of hydroxyl (*OH), oxyl (*O) and hydroperoxyl (*OOH) species on the catalyst surface followed by the formation of O_2 (* represents atoms adsorbed on the catalyst surface)[33]. For Ni- or Fe-based oxides, the conversion of *OH to *O is known to be the rate-determining step. On the other hand, vanadium oxide can easily convert *OH to *O but the conversion of *O to *OOH is slow[33,34]. Therefore, the co-presence of V, Fe and Ni on the film surface is expected to enable faster oxidation kinetics of water than FeOOH/NiOOH alone as vanadium can help to improve the kinetics of the rate-determining step by the FeOOH/NiOOH OEC. It has been shown experimentally and also by first-principle calculations that vanadium incorporation into the Ni-based layered double hydroxide can significantly lower the free-energy requirement for the formation of *O compared with Fe incorporation into the Ni-based layered double hydroxide[32].

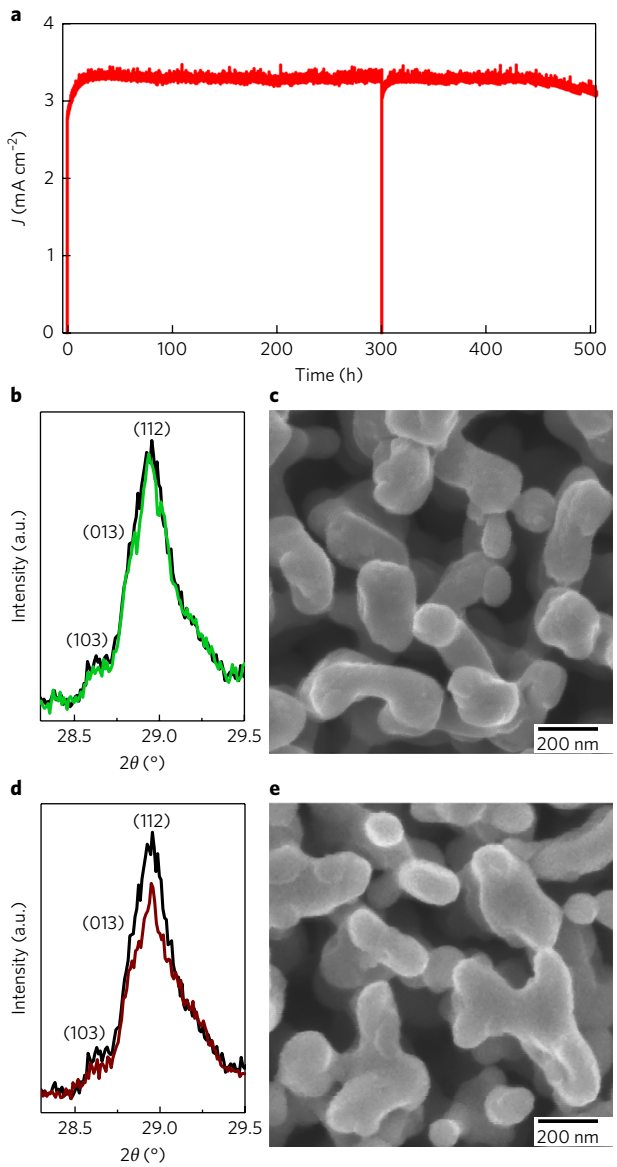

Fig. 5 | Long-term photostability test. a, *J*–*t* plot of the $BiVO_4$/FeOOH/NiOOH film in KB + V at 0.6 V versus RHE. **b**,**c**, XRD pattern (green) and SEM image of the $BiVO_4$/FeOOH/NiOOH film after 300 h. **d**,**e**, XRD pattern (brown) and SEM image of the $BiVO_4$/FeOOH/NiOOH film after 500 h. The XRD pattern of $BiVO_4$ before *J*–*t* measurement is shown in black for comparison in **b** and **d**.

We also found that the vanadium incorporated into the FeOOH/NiOOH film is not stable. If the FeOOH/NiOOH film containing vanadium is used for water oxidation in the KB solution, vanadium leaches out. Figure 4c shows the *J*–*t* plot of the FeOOH/NiOOH electrode in the KB + V solution for the initial 20 h and then in the KB solution for an additional 60 h. The increase in the current observed in the KB + V solution is due to the incorporation of vanadium and the decrease in the current observed after moving the electrode to the KB solution is due to the loss of vanadium from the film. We confirmed by EDS that the amount of vanadium present in the FeOOH/NiOOH film after 60 h of operation in the KB solution was negligible. This additional result supports the idea that the use of a vanadium-saturated solution may be an effective strategy to both suppress the photocorrosion of a photoanode that contains vanadium and ensure long-term stability of vanadium-containing catalysts if the loss of vanadium is the main problem for maintaining stability.

Photostability test of $BiVO_4$/FeOOH/NiOOH over 500 h

Figure 5a shows a *J*–*t* plot of the $BiVO_4$/FeOOH/NiOOH at 0.6 V versus RHE in the KB + V solution for 500 h, which demonstrates stable photocurrent generation up to 450 h. The XRD patterns and SEM images of the $BiVO_4$/FeOOH/NiOOH were taken at 300 h and at 500 h to investigate the mass loss of $BiVO_4$ during the *J*–*t* measurement. The XRD pattern and SEM image taken at 300 h show no detectable changes compared to those taken before the *J*–*t* measurement (Fig. 5b,c). However, the XRD pattern taken at 500 h shows a decrease in the peak intensity of $BiVO_4$ (Fig. 5d). The SEM image taken at 500 h (Fig. 5e) shows a change in surface morphology due to the deposition of a thicker Fe/Ni–V–O layer but serious dissolution damage to $BiVO_4$ like that shown in Supplementary Fig. 6b was not found. We noticed that the colour of $BiVO_4$ near the $BiVO_4$/FTO junction changed to brown, suggesting the formation of Bi metal, which is indicative of cathodic photocorrosion. Therefore, we suspect that the decrease in the XRD peak intensity and the decrease in photocurrent may be mostly associated with a different type of photocorrosion (that is, cathodic photocorrosion) occurring at the $BiVO_4$/FTO junction at the end of the 500 h *J*–*t* measurement. Further investigations and the development of strategies to suppress the photocorrosion at the $BiVO_4$/FTO junction will be the topic of a follow-up study.

Conclusions

In conclusion, we have demonstrated a strategy to suppress anodic photocorrosion of $BiVO_4$ using a V^{5+}-saturated electrolyte. The presence of V^{5+} species in the electrolyte inhibited the photooxidation-coupled dissolution of V^{5+} and prevented the anodic photocorrosion of $BiVO_4$. A strategy for preventing photocorrosion by the composition tuning of the electrolyte may potentially be used for other photoelectrodes that undergo a photocorrosion process coupled with a loss of an electrode component by dissolution. In addition, we discovered that the presence of V^{5+} species in the electrolyte can generate a vanadium-containing interfacial layer in situ on the FeOOH/NiOOH film that can enhance water-oxidation kinetics. Although this phase was not stable under conventional operating conditions for water oxidation due to vanadium loss, the use of a solution saturated with V^{5+} species allowed this phase to perform water oxidation in a stable manner. This study showed that employing an electrolyte that can suppress the loss of an active component of the photoelectrode and catalysts can be an effective method to enhance the long-term stability of photoelectrodes and catalysts that are highly active but do not have long-term stability under given operating conditions.

Methods

Electrochemical synthesis of BiOI films. BiOI electrodes were first electrodeposited to serve as precursor films to form nanoporous $BiVO_4$ electrodes. The mechanism and conditions for BiOI deposition were reported previously[13,14,35]. In this study, two major changes were made to deposit denser and more uniform BiOI films. The first change made was to increase the nucleation density of BiOI crystals in the initial stage of deposition and the second was to reduce the deposition current density used during the growth step. This allows the nuclei formed in the initial stage of deposition to grow uniformly and prevents new nucleation events from occurring on top of the initial layer of crystals during the growth step, resulting in more even film growth.

A typical plating solution was 50 ml of an aqueous solution containing 15 mM $Bi(NO_3)_3{\cdot}5H_2O$ (Aldrich, 98%), 400 mM KI (Aldrich, 99%) and 30 mM lactic acid (Alfa, 85–90%). The pH was adjusted to 1.8 by adding HNO_3 (Aldrich, 98%). To this solution, 20 ml of ethanol (Pharmco, 200 proof) containing 46 mM *p*-benzoquinone (Aldrich, 98%) was slowly added. A sudden addition of the ethanol solution can cause an abrupt increase in pH and induce precipitation of BiOI in the solution. The mixed solution was stirred for several minutes until its pH stabilized. The final pH was adjusted to 3.4 ± 0.05 by adding HNO_3.

A typical three-electrode cell was used for electrodeposition. A fluorine-doped tin oxide (FTO) working electrode (WE) (Hartford Glass), a Ag/AgCl (4 M KCl) reference electrode (RE) and a platinum counter electrode (CE) were used. The platinum CE was prepared by depositing 100 nm of platinum on top of a 20 nm titanium adhesion layer on a clean glass slide using electron-beam evaporation. A VMP2 multichannel potentiostat (Princeton Applied Research) was used for electrodeposition and all subsequent electrochemical studies.

The potentiostatic deposition was performed in two steps. For the nucleation step, a potential of −0.35 V versus Ag/AgCl was applied for 20 s. This potential is enough to reduce $[BiI_4]^-$ to Bi. The Bi nanoparticles deposited in this step served as nucleation sites for BiOI and increased the nucleation density of the BiOI plates (Supplementary Fig. 1).

After the initial nucleation step, a continuous potential of −0.10 V versus Ag/AgCl was applied for about 17 min to pass 0.37 C cm^{-2} for the growth step. This potential is not sufficient to reduce $[BiI_4]^-$ to Bi but can reduce *p*-benzoquinone to hydroquinone. This reaction increases the local pH on the WE and induces the deposition of BiOI (ref. [35]). To decrease the growth rate of BiOI, the concentrations of *p*-benzoquinone and Bi^{3+} ions used in this study were significantly lower than those used in previous studies[13,14]. In addition, the plating solution used in this study contained lactic acid. At pH 3.4, lactic acid is partially deprotonated and can serve as a buffer. The use of a lactate buffer solution enabled a more uniform increase in pH at the electrode/electrolyte interface during the reduction of *p*-benzoquinone, resulting in a more even growth of BiOI crystals throughout the film. Without the lactate buffer, some sites that generate higher current densities for *p*-benzoquinone reduction can rapidly increase the pH and cause irregular nucleation/growth of BiOI, resulting in the formation of an uneven surface. This modified method allowed us to increase the mass of BiOI per unit area without significantly increasing film thickness (Supplementary Fig. 1). The major difference in the deposition conditions in the previous and current study is summarized in Supplementary Table 1.

Conversion of BiOI films to $BiVO_4$ films and N_2-treatment. The BiOI electrodes were converted to $BiVO_4$ by a thermal treatment in air at 450 °C for 2 h (ramp rate = 2 °C min^{-1}) after covering the film surface (1.0 × 1.3 cm^2) with 50 µl cm^{-2} of a dimethyl sulfoxide (BDH, 99.9%) solution containing 200 mM $VO(acac)_2$ (Aldrich, 98%)[28]. After the conversion, excess V_2O_5 present in the $BiVO_4$ electrode was removed by soaking the film in 1 M NaOH (Aldrich, 97%) solution for 30 min with stirring (about 350 r.p.m.). The electrode was then thoroughly rinsed with deionized water and dried with an air stream.

A nitrogen treatment of $BiVO_4$ was performed by re-annealing the $BiVO_4$ electrode at 350 °C for 2 h (ramp rate = 5 °C min^{-1}) in a tube furnace while flowing N_2 (about 400 ml min^{-1})[13]. Before elevating the temperature, the tube furnace was purged with N_2 for more than 2 h to completely eliminate O_2 from the tube. The $BiVO_4$ electrode in the tube furnace was tilted about 40° upwards with respect to the horizontally positioned tube so that the surface of the $BiVO_4$ could face the N_2 flow.

The SEM images of the resulting $BiVO_4$ electrodes are shown in Supplementary Fig. 2. The average particle size was increased to 110 ± 30 nm compared with that of $BiVO_4$ (76 ± 5 nm) prepared using the previously reported conditions. In addition, the film thickness increased from 0.7 ± 0.1 µm to 1.1 ± 0.1 µm as more charge was passed to deposit these BiOI films. The columnar growth of $BiVO_4$ under these conditions minimizes grain boundaries, ensuring good electron transport to the back contact.

Photodeposition of FeOOH/NiOOH OECs on $BiVO_4$ electrodes. The rationale for using dual layers of FeOOH and NiOOH oxygen-evolution catalysts (OECs) on $BiVO_4$ electrodes (that is, the deposition of FeOOH on $BiVO_4$ followed by the deposition of NiOOH on FeOOH) and the photodeposition mechanisms of FeOOH and NiOOH have been reported previously[14]. The $BiVO_4$ electrodes used in this study were N_2-treated and, as a result, possessed hydrophobic surfaces that cannot be easily wetted[13]. Therefore, before the OEC deposition, the $BiVO_4$ electrodes were immersed in 1.0 M borate buffer solution (pH 9.3) containing 0.2 M Na_2SO_3 and, using the $BiVO_4$ electrode as the WE, the potential was swept between the open-circuit potential and 0.45 V versus Ag/AgCl under 1 sun illumination. This procedure was repeated at least five times until the anodic photocurrents generated for sulfite oxidation converged. This process serves as an activation step to form a hydrophilic surface without damaging the electrode. The electrode was then rinsed with deionized water and dried with an air stream. After this process, the $BiVO_4$ electrodes were ready for photodeposition of OEC layers. As the morphology and the thickness of $BiVO_4$ used in this study are different from those used in the previous study, a few modifications were also made to re-optimize the deposition conditions of FeOOH/NiOOH.

For FeOOH deposition, the major modifications made include the use of a more dilute Fe^{2+} plating solution, more intense light and a more positive applied potential. Fe^{2+} ions present in the plating solution gradually precipitate as FeOOH in the bulk solution due to the oxidation of Fe^{2+} by O_2 in the air. This constantly changes the concentration of Fe^{2+} ions available for photodeposition of FeOOH on $BiVO_4$, creating a source of irreproducibility for FeOOH deposition. Therefore, we chose to use a more dilute Fe^{2+} solution to reduce bulk precipitation of FeOOH by O_2. To compensate for the effect of a decreased Fe^{2+} concentration on the photodeposition rate, a higher light intensity and a more positive potential was used for the photodeposition of FeOOH. Another major change was a decrease in the charge passed during the photodeposition. Depositing a thicker OEC film can be favourable for decreasing the probability of having pinholes present in the OEC layer; however, having a thicker, non-conductive oxyhydroxide OEC layer can decrease the fill factor of $BiVO_4$ during a *J*–*V* scan. Therefore, we identified an optimum amount of charge to pass to deposit a thinner OEC layer, which increased the fill factor, while maintaining the OEC coating quality.

FeOOH was photodeposited from 60 ml of deionized water containing 5 mM $FeSO_4{\cdot}7H_2O$ (Aldrich, 99%) and 100 mM K_2SO_4 (Aldrich, 99%). The pH of the solution was 5.3 ± 0.2 without any adjustment. Before dissolving the solutes, deionized water was purged with N_2 gas for 30 min to remove dissolved oxygen from the solution. The light intensity at the FTO surface was adjusted to be 3 mW cm^{-2} using neutral-density filters (Newport, UV-grade fused silica). The surface-activated $BiVO_4$ electrode was used as the WE in an undivided three-electrode cell. While stirring, an anodic bias of 0.139 V versus Ag/AgCl was applied to the WE in the dark and, after the dark current was stabilized below 3 µA cm^{-2}, the WE was illuminated through the back-side for about 150 s to pass 8.3 mC cm^{-2}. The photocurrent density observed during deposition was 110–160 µA cm^{-2}. After the deposition, the electrode was rinsed with deionized water and the moisture was removed by a gentle stream of air. Then, the film was air-dried for at least 3 h in a well-ventilated fume hood before NiOOH deposition.

The oxidation of Ni^{2+} to Ni^{3+} is more difficult than that of Fe^{2+} and, therefore, depositing a uniform NiOOH layer on the nanoporous $BiVO_4$ surface is more challenging. In general, before achieving good coverage of NiOOH within the porous structure of $BiVO_4$, an undesirably thick NiOOH layer can form on the film surface. This is because NiOOH deposition within the porous structure is considerably limited by the mass transport of Ni^{2+} after the initial depletion of Ni^{2+} at the electrode surface. To overcome this issue, the $BiVO_4$/FeOOH electrode was soaked in a 50 mM $NiSO_4{\cdot}6H_2O$ (Aldrich, 99%) aqueous solution for 5 min before photodeposition so that the nanopores of the $BiVO_4$/FeOOH electrode were pre-filled with the Ni^{2+} solution by capillary action. Then, the $BiVO_4$/FeOOH electrode was moved from the Ni^{2+}-containing solution to a 100 mM K_2SO_4 aqueous solution (pH 8.0 ± 0.3, adjusted using diluted KOH solution) without any Ni^{2+} ions and photodeposition of NiOOH was initiated immediately. During photodeposition, the Ni^{2+} ions within the pores can gradually diffuse out to the solution and this method creates a unique situation where the Ni^{2+} concentration in the pores is higher than that on the film surface during photodeposition. After consuming the majority of Ni^{2+} ions within the pores, the procedure was repeated one more time to refill the pores with Ni^{2+} ions and perform photodeposition of NiOOH. The same illumination condition used for FeOOH deposition was used and 0.029 V versus Ag/AgCl was applied for 70 s without stirring to pass 2.1 mC cm^{-2} for each deposition. (Therefore, the total charge passed to deposit NiOOH was 4.2 mC cm^{-2}.) After the deposition, the electrode was rinsed with deionized water and the moisture was removed by a gentle stream of air. Then the film was air-dried for at least 24 h in a well-ventilated fume hood before use.

Since the photodeposited FeOOH/NiOOH layers are extremely thin, no changes were evident in the surface morphology during SEM studies (Supplementary Fig. 4). However, the EDS analysis confirmed the presence of Fe and Ni on the $BiVO_4$ surface with the atomic ratio of 9:1. The major differences between the photodeposition methods used in the previous and the current study are summarized in Supplementary Table 2.

Deposition of FeOOH/NiOOH OECs on FTO. FeOOH/NiOOH OECs were electrodeposited on FTO substrates to perform control experiments discussed in the main text. The same three-electrode set-up in an undivided cell described above for the deposition of BiOI was used. For the deposition of FeOOH, a plating solution was prepared by dissolving 5 mM $FeSO_4{\cdot}7H_2O$ in 60 ml of 100 mM K_2SO_4 aqueous solution at 70 °C (pH was not adjusted) after purging the solution with N_2 for 30 min. Immediately after the $FeSO_4{\cdot}7H_2O$ was dissolved, a potential of 1.2 V versus Ag/AgCl was applied to an FTO working electrode for 1 min (about 30 mC cm^{-2}) to anodically deposit a FeOOH film. After deposition, the film was rinsed with deionized water and the moisture was removed by a gentle stream of air. Then, the film was air-dried for 3 h in a well-ventilated fume hood before NiOOH deposition.

The NiOOH was deposited on the FTO/FeOOH WE from a 100 mM K_2SO_4 solution containing 15 mM $NiSO_4{\cdot}6H_2O$ at 70 °C. The pH was adjusted to 7.2 ± 0.3 using dilute KOH solution before heating. An anodic bias of 1.2 V versus Ag/AgCl was applied for 10 min (about 450 mC cm^{-2}). The same deposition process was repeated one more time after rinsing, removing moisture and air-drying the film in the fume hood for 1 h. After the deposition, the electrode was rinsed with deionized water and air-dried for 24 h in a well-ventilated fume hood before use.

Characterization. The crystallinity and purity of $BiVO_4$ electrodes were examined by a Bruker D8 Advanced X-ray diffractometer (Ni-filtered Cu K_α radiation, $\lambda = 1.5418$ Å) (Supplementary Fig. 3). The morphology of the electrodes was examined using a LEO 1530 Gemini SEM with an accelerating voltage of 2–5 keV. The elemental analysis of the electrodes was performed using a Thermo Scientific

UltraDry EDS detector with an accelerating voltage of 15 keV. The elemental analysis of the electrolytes was carried out using inductively coupled plasma optical emission spectrometry (Perkin Elmer Optima 2000 ICP–OES). For the ICP–OES measurement, the electrolyte was diluted by a factor of two by adding deionized water, and 100 ppb yttrium was added as an internal standard. The element concentration was calibrated using 50, 100 and 500 ppb ICP standard solutions (Aldrich 05719 (Bi), 18399 (V), 43149 (Fe), 28944 (Ni) and 01357 (Y)). For the KB + V solution, since the intense peak of V interfered with the baselines of Bi, Fe and Ni spectra, the baselines of the Bi, Fe and Ni spectra were manually determined and subtracted for more accurate quantification of Bi, Fe and Ni.

Photoelectrochemical measurements. In general, photoelectrochemical measurements were performed according to our recent protocol paper[28]. Detailed conditions used in this study are as follows. A three-electrode configuration in an undivided quartz cell was used with a BioLogic SP-200 potentiostat. A platinum wire (Aldrich, 99.9%) CE and a Ag/AgCl (4 M KCl) RE were used. The conversion of the potential measured versus the Ag/AgCl (4 M KCl) RE to the potential versus RHE (reversible hydrogen electrode) was achieved using the equation below.

$$E(\text{versus RHE}) = E(\text{versus Ag/AgCl}) + E_{\text{Ag/AgCl}}(\text{reference}) + 0.0591\ \text{V} \times \text{pH}$$

$$\left(E_{\text{Ag/AgCl}}(\text{reference}) = 0.1976\ \text{V versus NHE at } 25^{\circ}\text{C}\right)$$

The light was generated from a 300 W Xe arc lamp (Ushio, UXL-302-0) and passed through an air mass 1.5 global (AM 1.5 G) filter, an infrared (water) filter (Newport) and neutral-density filters. Then, the light was guided to the quartz cell using a bundle of optical fibres with a collimating lens (Newport) at the end of the bundle. Illumination was through the FTO side of the $BiVO_4$/FeOOH/NiOOH electrode (back-side illumination). The intensity of the light was calibrated to be one sun (100 mW cm^{-2}) at the surface of the FTO substrate (before the light passes through the FTO) using a NREL-certified GaAs reference cell (PV Measurement). For the long-term stability and gas-detection experiments, an Oriel LCS-100 solar simulator (100 W Xe arc lamp) equipped with an AM 1.5 G filter was used without an optical fibre bundle to allow for illumination of a larger area of the sample. An infrared filter, a focusing lens and neutral-density filters were placed between the light source and the sample to prevent heating of the electrolyte and to achieve 100 mW cm^{-2} illumination.

The $BiVO_4$/FeOOH/NiOOH electrodes used for general photocurrent measurements were masked using acrylates copolymer (clear nail polish) to expose a uniform area of about 0.06 cm^2. For long-term stability tests that involved continuous O_2 evolution for more than 60 h, a more durable masking was necessary. For these studies, a copper wire was soldered to the FTO electrode and an epoxy adhesive (J-B weld) was applied to the soldered Cu wire, any exposed FTO substrate, and the edge-sides of the $BiVO_4$/FeOOH/NiOOH electrode to expose about 0.2 cm^2 of the $BiVO_4$/FeOOH/NiOOH electrode. The epoxy was then cured for one day.

The KB solution used for photocurrent measurement was 60 ml of a 1.0 M borate buffer solution, which was prepared by dissolving 1.0 M H_3BO_3 (Aldrich, 99.5%) in deionized water (18 MΩ) and adjusting the pH to be 9.3 using KOH (Aldrich, 85%). The KB + V solution was prepared by dissolving 0.1 M V_2O_5 (Aldrich, 98%) in the KB solution at 60 °C for 3 h with rapid stirring. After dissolution, the pH was re-adjusted to 9.3 by adding KOH, and the solution was stirred for one day before use. All linear sweep voltammetry scans were performed from the open-circuit potential to the positive direction with a scan rate of 10 mV s^{-1}. For long-term (>60 h) *J*–*t* measurements, 500 ml of an electrolyte solution was used and after every 24 h, 50% of the electrolyte was replaced with a new buffer solution. The solution was purged with N_2 during both the *J*–*V* and *J*–*t* measurements.

For the *J*–*V* measurement for sulfite oxidation, 60 ml of a KB buffer containing 0.2 M Na_2SO_3 (Aldrich, 98%) was used. For the 500 h *J*–*t* measurement for sulfite oxidation, 1.0 l of a KB buffer containing 0.7 M sulfite was used to avoid depletion of sulfite within a few days. The concentration of KB was decreased to 0.5 M to achieve higher solubility of sulfite. The electrolyte was replaced with a new KB solution containing sulfite at 200 and 300 h.

H_2 and O_2 gas detection was performed by applying 0.6 V versus RHE using a three-electrode set-up in a gas-tight divided cell with a glass frit. The electrolyte was not stirred to prevent oxygen diffusion from the WE compartment to the CE compartment, which may cause oxygen reduction to occur at the Pt CE. The size of the $BiVO_4$/FeOOH/NiOOH electrode used for this experiment was about 1.2 cm^2. The H_2 gas was detected using a gas chromatograph–mass spectrometer (Shimazu, GCMS-QP2010 Ultra) equipped with a ShinCarbon ST packed column (Restek) and a secondary electron detector. He (99.9997%) was used as the carrier gas. The amount of H_2 evolution was determined by sampling 100 µl of gas from the headspace of the CE compartment using a gas-tight syringe every 1 h. The O_2 gas was detected using an Ocean Optics fluorescence-based oxygen sensor (Neofox, FOSPOR-R). The probe was inserted into the headspace of the WE side, and the vol% of evolved O_2 was continuously recorded. The amount of O_2 evolution was determined after adjusting for the dissolved O_2 in the electrolyte of the WE side using Henry's law[28]. The Faradaic efficiency was calculated by dividing the amount of gas detected by the theoretical amount of gas calculated on the basis of the total charge passed, using the following equation

$$\text{FE}(\%) = \frac{A \times n(\text{mol}) \times F(\text{C mol}^{-1})}{\text{Charge passed through WE (C)}} \times 100$$

where n is moles of evolved H_2 or O_2 gas, A is the number of electrons required to generate one H_2 or O_2 molecule (two for H_2, four for O_2) and F is the Faraday constant (96485.33 C mol^{-1}).

Data availability. The data that support the plots within this paper and other findings of this study are available from the corresponding author upon reasonable request.

Received: 28 June 2017; Accepted: 10 November 2017;
Published online: 18 December 2017

References

1. Kudo, A., Omori, K. & Kato, H. A novel aqueous process for preparation of crystal form-controlled and highly crystalline $BiVO_4$ powder from layered vanadates at room temperature and its photocatalytic and photophysical properties. *J. Am. Chem. Soc.* **121**, 11459–11467 (1999).
2. Sayama, K. et al. Photoelectrochemical decomposition of water into H_2 and O_2 on porous $BiVO_4$ thin-film electrodes under visible light and significant effect of Ag ion treatment. *J. Phys. Chem. B* **110**, 11352–11360 (2006).
3. Park, Y., McDonald, K. J. & Choi, K.-S. Progress in bismuth vanadate photoanodes for use in solar water oxidation. *Chem. Soc. Rev.* **42**, 2321–2337 (2013).
4. Sivula, K. & van de Krol, R. Semiconducting materials for photoelectrochemical energy conversion. *Nat. Rev. Mater.* **1**, 15010 (2016).
5. Park, H. S. et al. Factors in the metal doping of $BiVO_4$ for improved photoelectrocatalytic activity as studied by scanning electrochemical microscopy and first-principles density-functional calculation. *J. Phys. Chem. C* **115**, 17870–17879 (2011).
6. Liang, Y., Tsubota, T., Mooij, L. P. A. & van de Krol, R. Highly improved quantum efficiencies for thin film $BiVO_4$ photoanodes. *J. Phys. Chem. C* **115**, 17594–17598 (2011).
7. Parmar, K. P. S. et al. Photocatalytic and photoelectrochemical water oxidation over metal-doped monoclinic $BiVO_4$ photoanodes. *ChemSusChem* **5**, 1926–1934 (2012).
8. Luo, W. et al. Solar hydrogen generation from seawater with a modified $BiVO_4$ photoanode. *Energy Environ. Sci.* **4**, 4046–4051 (2011).
9. Park, Y., Kang, D. & Choi, K.-S. Marked enhancement in electron-hole separation achieved in the low bias region using electrochemically prepared Mo-doped $BiVO_4$ photoanodes. *Phys. Chem. Chem. Phys.* **16**, 1238–1246 (2014).
10. Seabold, J. A., Zhu, K. & Neale, N. R. Efficient solar photoelectrolysis by nanoporous Mo:$BiVO_4$ through controlled electron transport. *Phys. Chem. Chem. Phys.* **16**, 1121–1131 (2014).
11. Jo, W. J. et al. Phosphate doping into monoclinic $BiVO_4$ for enhanced photoelectrochemical water oxidation activity. *Angew. Chem. Int. Ed.* **51**, 3147–3151 (2012).
12. Wang, G. et al. Computational and photoelectrochemical study of hydrogenated bismuth vanadate. *J. Phys. Chem. C* **117**, 10957–10964 (2013).
13. Kim, T. W., Ping, Y., Galli, G. A. & Choi, K.-S. Simultaneous enhancements in photon absorption and charge transport of bismuth vanadate photoanodes for solar water splitting. *Nat. Commun.* **6**, 8769 (2015).
14. Kim, T. W. & Choi, K.-S. Nanoporous $BiVO_4$ photoanodes with dual-layer oxygen evolution catalysts for solar water splitting. *Science* **343**, 990–994 (2014).
15. Kuang, Y. et al. A front-illuminated nanostructured transparent $BiVO_4$ photoanode for >2% efficient water splitting. *Adv. Energy Mater.* **6**, 1501645 (2016).
16. Zhong, D. K., Choi, S. & Gamelin, D. R. Near-complete suppression of surface recombination in solar photoelectrolysis by "Co-Pi" catalyst-modified W:$BiVO_4$. *J. Am. Chem. Soc.* **133**, 18370–18377 (2011).
17. Seabold, J. A. & Choi, K.-S. Efficient and stable photo-oxidation of water by a bismuth vanadate photoanode coupled with an iron oxyhydroxide oxygen evolution catalyst. *J. Am. Chem. Soc.* **134**, 2186–2192 (2012).
18. Lichterman, M. F. et al. Enhanced stability and activity for water oxidation in alkaline media with bismuth vanadate photoelectrodes modified with a cobalt oxide catalytic layer produced by atomic layer deposition. *J. Phys. Chem. Lett.* **4**, 4188–4191 (2013).
19. Abdi, F. F. et al. Efficient solar water splitting by enhanced charge separation in a bismuth vanadate–silicon tandem photoelectrode. *Nat. Commun.* **4**, 2195 (2013).

20. Chen, Y.-S., Manser, J. S. & Kamat, P. V. All solution-processed lead halide perovskite-$BiVO_4$ tandem assembly for photolytic solar fuels production. *J. Am. Chem. Soc.* **137**, 974–981 (2015).
21. Pihosh, Y. et al. Photocatalytic generation of hydrogen by core-shell WO_3/$BiVO_4$ nanorods with ultimate water splitting efficiency. *Sci. Rep.* **5**, 11141 (2015).
22. Kim, J. H. et al. Hetero-type dual photoanodes for unbiased solar water splitting with extended light harvesting. *Nat. Commun.* **7**, 13380 (2016).
23. Kuang, Y. et al. Ultrastable low-bias water splitting photoanodes via photocorrosion inhibition and in situ catalyst regeneration. *Nat. Energy* **2**, 16191 (2016).
24. Bae, D. et al. Strategies for stable water splitting via protected photoelectrodes. *Chem. Soc. Rev.* **46**, 1933–1954 (2017).
25. Kohl, P. A., Frank, S. N. & Bard, A. J. Semiconductor electrodes: XI. Behavior of n-and p-type single crystal semiconductors covered with thin films. *J. Electrochem. Soc.* **124**, 225–229 (1977).
26. Paracchino, A. et al. Highly active oxide photocathode for photoelectrochemical water reduction. *Nat. Mater.* **10**, 456–461 (2011).
27. Gissler, W., McEvoy, A. J. & Graetzel, M. The effect of sputtered RuO_2 overlayers on the photoelectrochemical behavior of CdS electrodes. *J. Electrochem. Soc.* **129**, 1733–1736 (1982).
28. Govindaraju, G. V., Wheeler, G. P., Lee, D. & Choi, K.-S. Methods for electrochemical synthesis and photoelectrochemical characterization for photoelectrodes. *Chem. Mater.* **29**, 355–370 (2017).
29. Toma, F. M. et al. Mechanistic insights into chemical and photochemical transformations of bismuth vanadate photoanodes. *Nat. Commun.* **7**, 12012 (2016).
30. Pourbaix, M. *Atlas of Electrochemical Equilibria in Aqueous Solutions* (National Association of Corrosion Engineers, Houston, 1974).
31. Kanan, M. W., Surendranath, Y. & Nocera, D. G. Cobalt-phosphate oxygen-evolving compound. *Chem. Soc. Rev.* **38**, 109–114 (2009).
32. Fan, K. et al. Nickel–vanadium monolayer double hydroxide for efficient electrochemical water oxidation. *Nat. Commun.* **7**, 11981 (2016).
33. Man, I. C. et al. Universality in oxygen evolution electrocatalysis on oxide surfaces. *ChemCatChem* **3**, 1159–1165 (2011).
34. Diaz-Morales, O., Ledezma-Yanez, I., Koper, M. T. M. & Calle-Vallejo, F. Guidelines for the rational design of Ni-based double hydroxide electrocatalysts for the oxygen evolution reaction. *ACS Catal.* **5**, 5380–5387 (2015).
35. McDonald, K. J. & Choi, K.-S. A new electrochemical synthesis route for a BiOI electrode and its conversion to a highly efficient porous $BiVO_4$ photoanode for solar water oxidation. *Energy Environ. Sci.* **5**, 8553–8557 (2012).

Acknowledgements

This work was supported by the National Science Foundation (NSF) under the NSF Center CHE-1305124. The authors thank D.-H. Nam for his valuable suggestions and discussion for the study.

Author contributions

K.-S.C. and D.K.L. planned the experiments, interpreted the experimental results and wrote the manuscript. D.K.L. performed all experiments and K.-S.C. supervised the project.

Competing interests

The authors declare no competing financial interests.

Additional information

Supplementary information is available for this paper at https://doi.org/10.1038/s41560-017-0057-0.

Reprints and permissions information is available at www.nature.com/reprints.

Correspondence and requests for materials should be addressed to K.-S.C.

Publisher's note: Springer Nature remains neutral with regard to jurisdictional claims in published maps and institutional affiliations.